ARTICLE NO. 78-201R

Behavior of a Turbulent Boundary Layer Subjected to Sudden Transverse Strain

Hiroshi Higuchi*
Dynamics Technology, Inc., Torrance, Calif.
and
Morris W. Rubesin†
NASA Ames Research Center, Moffett Field, Calif.

Data from two experiments on the development of Reynolds stress tensor components after a sudden application of transverse strain are compared with computations based on four turbulence models: a first-order mixing length model, a second-order two-equation eddy viscosity model, and two second-order Reynolds stress models. The second-order models do not produce dramatic improvements over the simple model. The Reynolds stress models still need development to represent the physics of shear-strained turbulence. The assumption of a scalar eddy viscosity is shown to be quite reasonable.

Nomenclature

a = dissipation rate modeling coefficient, Eq. (36)
A = van Driest damping length
b = dissipation rate modeling coefficient, Eq. (36)
C_{fx} = axial skin-friction coefficient, $C_{fx} = \tau_{wx} / \frac{1}{2}\rho u_e^2$
$C_{f\theta}$ = transverse skin-friction coefficient, $C_{f\theta} = -\tau_{w\theta} / \frac{1}{2}\rho u_e w_s$
C_1, C_2, C_3, C_4 = modeling coefficients, Eq. (36)
D = diameter of cylinder
e = specific kinetic energy of turbulence, Eq. (23)
J = magnitude of the mean rate of strain in a spinning boundary layer
ℓ = length scale, Eq. (27)
ℓ_i = mixing length in the inner portion of a boundary layer
p = static pressure
q = velocity scale, $q = \sqrt{2e}$
r = distance from axis of cylinder in cylindrical coordinate system
r_w = radius of cylinder
R_e, R_w = modeling coefficients (low turbulence Reynolds numbers), Eq. (27) or Eq. (38)
R_{eD} = Reynolds number based on body diameter, $u_e D/\nu$
Re_T = turbulence Reynolds numbers, Eq. (27)
$R_{\theta k}$ = Reynolds number based on momentum thickness utilizing axial component of velocity, $u_e \theta_k / \nu$
S_{ij} = mean rate of strain tensor, Eq. (17)
u, v, w or u_1, u_2, u_3 = components of the mean velocities in cylindrical coordinate system
x = distance along axis of cylinder measured from the junction
u', v', w' or u_1', u_2', u_3' = components of the instantaneous fluctuating velocities in cylindrical coordinate system
u_e = mainstream velocity
w_s = transverse surface velocity of the rotating cylinder
α = Clauser constant
β = function defined by Eq. (13)
β = modeling coefficient, Eq. (27) or Eq. (38)
β^* = modeling coefficient, Eq. (27) or Eq. (38)
γ = modeling coefficint, Eq. (27) or Eq. (38)
γ = intermittency, Eq. (15)
γ^* = eddy viscosity modeling coefficient, Eq. (27)
δ_{ij} = Kronecker delta
δ_{k^*} = displacement thickness based on axial velocity, Eq. (14)
δ_0 = boundary-layer thickness ahead of junction
δ_x = axial boundary-layer thickness where $u = 0.99\, u_e$
δ_θ = transverse boundary-layer thickness where $w = 0.01\, w_s$
ϵ = eddy viscosity (kinematic) or eddy diffusivity
κ = Karman constant, 0.4
λ = modeling coefficient, Eq. (27) or Eq. (38)
λ^* = modeling coefficient, Eq. (38)
Λ = length scale, Eq. (34)
ν = kinematic viscosity
$\tilde{\pi}$ = function defined by Eq. (12)
σ = modeling coefficient, Eq. (27)
σ_1 = modeling coefficient, Eq. (36)
σ^* = modeling coefficient, Eq. (38)
τ_w = surface skin friction
χ = modeling rate of strain parameter, Eq. (38)
ω = pseudovorticity, Eq. (26)
Ω = dimensionless rotation rate, $\Omega = w_s / u_e$

Subscripts

e = at edge of the boundary layer
i = inner region of a boundary layer

Presented as Paper 78-201 at the AIAA 16th Aerospace Sciences Meeting, Huntsville, Ala., Jan. 16-18, 1978; submitted Feb. 21, 1978; revision received March 1, 1979. This paper is declared a work of the U.S. Government and therefore is in the public domain. Reprints of this article may be ordered from AIAA Special Publications, 1290 Avenue of the Americas, New York, N.Y. 10019. Order by Article No. at top of page. Member price $2.00 each, nonmember, $3.00 each. **Remittance must accompany order.**

Index category: Boundary Layers and Convective Heat Transfer—Turbulent.

*Research Scientist. Member AIAA.
†Sr. Staff Scientist. Associate Fellow AIAA.

o = outer region of a boundary layer
0 = station upstream of the junction
x = property of boundary layer along axis of cylinder
w = at the surface
∞ = modeling coefficient value as turbulence Reynolds number $\to \infty$
θ = property of transverse boundary layer

Introduction

THE response of an established two-dimensional turbulent boundary layer to a suddenly applied transverse surface shear is particularly sensitive to the rates of interaction between the individual components of the Reynolds stress tensor. An understanding of these mechanisms is important for the prediction of the behavior of three-dimensional turbulent flowfields.[1] These mechanisms have been investigated in two well-documented experiments[2,3] where the boundary layer grew on a cylinder with its axis in the freestream direction of a low-speed wind tunnel. The cylinder was segmented in a plane perpendicular to its axis, and the downstream portion of the cylinder was rotated about its axis. The boundary layer on the rotating portion of the cylinder provided the test zone responding to the sudden imposition of transverse shear.

One of these experiments[2] was the object of a numerical analysis that employed an algebraic eddy viscosity model to describe the turbulence.[4] The model employed was a logical extension of the Cebeci-Smith model.[5] Extension of the model to the rotating boundary layer was accomplished with the assumptions that the eddy viscosity is a scalar and that its magnitude in the wall region is determined by the resultant rate of mean strain.

Since 1974, the Ames Research Center has been involved with turbulent boundary-layer computer codes developed by the Aeronautical Research Associates of Princton (ARAP) and DCW Industries. The authors have compared these codes with a variety of experiments and participated in their modification and improvement. One code by DCW is based on a two-equation model for turbulence kinetic energy and pseudovorticity (or frequency scale) that, together, establish an eddy viscosity. Although this eddy viscosity is still a scalar, it is expected to reflect the dynamics of the turbulence generation over the rotating cylinder. Two other codes, one each by ARAP and DCW, employ models for the dynamics of the individual components of the Reynolds stress tensor. In this paper, these codes are applied to the conditions of the experiments of Refs. 2 and 3. These computations, along with the algebraic eddy viscosity computations of Ref. 4, provide a means of assessing the level of models required to describe a suddenly disturbed quasi-three-dimensional boundary layer.

Description of the Experiments

Both experiments used a similar flow configuration, indicated schematically in Fig. 1 where the boundary-layer thicknesses are exaggerated for clarity. The test boundary layer is produced on a circular cylinder with its axis parallel to the freestream direction. The cylinder is segmented and the downstream segment is rotated about the axis at various surface speed ratios Ω with respect to the freestream velocity. An axisymmetric, fully developed turbulent boundary layer at the end of the stationary cylinder encounters a sudden transverse rate of strain due to the rotation of the downstream cylinder. A transverse boundary layer, initiated there, is significantly thinner than the axial boundary layer for some distance. As the transverse boundary layer develops, a re-equilibrium process occurs among the components of the Reynolds stresses. Far downstream, the mean flow will relax into a collateral condition where the flow is planar when observed from the coordinate system fixed on the rotating body. Near the sudden strain, the components of the Reynolds stress tensor are still distributed approximately as they would be in a nonrotating cylinder. The rate of change between this initial and the collateral conditions provides information regarding the dynamic mechanisms governing the exchange among the individual components of the Reynolds stress tensor. These mechanisms represent the effects of the correlation between pressure and velocity strain rate fluctuations, major elements of the various turbulence models. These experiments, therefore, provide valuable information for assessing these models.

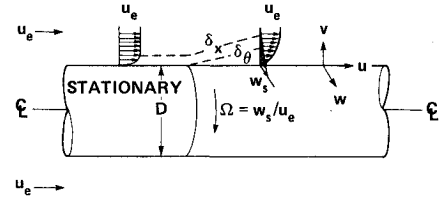

Fig. 1 Flow configuration under investigation.

The flow parameters and quantities measured in each experiment are listed in Table 1. Both experiments include data for each component of Reynolds stress tensor as well as the mean velocity profiles. Skin friction on the body surface was deduced from the measurements within the boundary layer. Hot-wire measurements of mean and fluctuating velocities in the highly skewed boundary layer imposed considerable difficulties on both experiments. For stations immediately downstream of the sudden transverse strain and for a higher surface velocity, Reynolds stress measurements are either unavailable or subject to a larger experimental uncertainty. In neither experiment did the measurements extend far enough downstream to show the equilibrium collateral condition. The experimental results at the lower rotation speeds are emphasized in the discussion.

Turbulence Models and Computer Codes

The equations of motion describing the boundary-layer development on the cylinder, for an incompressible fluid, are as follows:

Table 1 Flow parameters of the experiments

Experiments	Bissonnette and Mellor[2]	Lohmann[3]
Freestream velocity, u_e, m/s	19.4 or 10.1	16.8
Rotation rate, $\Omega = w_s/u_e$	0.936 or 1.80	1.45 or 2.20
Body diameter, D, cm	12.7	26.8
Reynolds number based on body diameter, Re_D	1.6×10^5 or 8.3×10^4	2.9×10^5
Boundary-layer thickness ahead of the segment, δ_0, cm	1.6 or 1.8	2.0
Measured quantities	u, w $\overline{u'^2}$, $\overline{v'^2}$, $\overline{w'^2}$ $\overline{u'v'}$, $\overline{v'w'}$, $\overline{u'w'}$	u, w $\overline{u'^2}$, $\overline{v'^2}$, $\overline{w'^2}$ $\overline{u'v'}$, $\overline{v'w'}$, $\overline{u'w'}$ ($\Omega = 1.45$ case only)

Continuity

$$\frac{\partial(ru)}{\partial x}+\frac{\partial(rv)}{\partial r}=0 \tag{1}$$

Momentum in the freestream direction

$$u\frac{\partial u}{\partial x}+v\frac{\partial u}{\partial r}=-\frac{1}{\rho}\frac{\partial p}{\partial x}+\frac{1}{r}\frac{\partial}{\partial r}\left[r\left(\nu\frac{\partial u}{\partial r}-\overline{u'v'}\right)\right] \tag{2}$$

Momentum in the circumferential direction

$$u\frac{\partial w}{\partial x}+\frac{v}{r}\frac{\partial(rw)}{\partial r}=\frac{1}{r^2}\frac{\partial}{\partial r}\left[r^2\left(\nu\left(\frac{\partial w}{\partial r}-\frac{w}{r}\right)-\overline{v'w'}\right)\right] \tag{3}$$

Momentum normal to the surface

$$\frac{1}{\rho}\frac{\partial p}{\partial r}=-\frac{1}{r}\frac{\partial}{\partial r}(r\overline{v'^2})+\frac{w^2}{r}+\frac{\overline{w'^2}}{r} \tag{4}$$

These equations allow for a thick boundary layer relative to the body radius.

The boundary conditions for Eqs. (1-4) are

$$\text{at } r=r_w \quad u=v=0, \quad w=w_s \tag{5a}$$

$$\text{as } r\to\infty \quad u\to u_e, \quad w\to 0, \quad p\to p_e \tag{5b}$$

In general, u_e and p_e vary along the body and are related by the Euler relation. The local pressure can be found from the boundary-layer edge pressure and Eq. (4).

In the four computational methods, different simplifications of these equations have been made, either to simplify the numerical methods or to conform to the requirements of particular turbulence models as indicated in their description. In the order of increasing complexity, the computer codes and models are as follows:

1) Aguilar numerical computational method[4] utilizing an extended Cebeci-Smith two-layer algebraic isotropic eddy viscosity model.[5]

2) A computer code developed by Wilcox (DCW) utilizing the Wilcox-Rubesin, two-equation isotropic eddy viscosity model.[6]

3) A computer code developed by Sullivan[7] (ARAP) utilizing Donaldson invariant tensor modeling.[8]

4) A computer code developed by Wilcox (DCW) utilizing the Wilcox-Rubesin Reynolds stress equation model.[6]

Aguilar Mixing Length Model

Aguilar developed a computer code to solve a set of equations equivalent to the complete set of Eqs. (1-4). The numerical scheme extends the computational field to the surface, in contrast to some computational schemes that avoid the use of fine mesh resolution near the surface by invoking a "law-to-the-wall" to which the numerical results are then forced. This is particularly important in dealing with rotating boundary layers because the appropriate law-of-the-wall for the boundary layer relaxing the suddenly applied transverse strain is not known a priori. The turbulence model utilized in these computations is a direct extension to the Cebeci model.[9] The model divides the turbulent boundary layer into two regions: the inner wall region (the sublayer, buffer layer, and logarithmic region) and the outer wake region. In the inner region, the mixing length is represented as

$$\ell_i=\kappa r_w \ell_n\left(\frac{r}{r_w}\right)\left[1-\exp\left(-\frac{r_w}{A}\ell_n\left(\frac{r}{r_w}\right)\right)\right]\left(\frac{r}{r_w}\right)^{1/2} \tag{6}$$

and the corresponding eddy viscosity is

$$\epsilon_i=\ell_i^2 J \tag{7}$$

Here J is the magnitude of the mean rate of strain in a spinning boundary layer:

$$J=\sqrt{\left(\frac{\partial u}{\partial r}\right)^2+\left(\frac{\partial w}{\partial r}-\frac{w}{r}\right)^2} \tag{8}$$

The quantity A is the van Driest damping length which, in the absence of strong pressure gradients or surface mass blowing, can be written as

$$A=26\sqrt{\nu/J_w} \tag{9}$$

where J_w represents the total rate of strain at the surface. Equations (6-9) completely define the inner layer eddy viscosity ϵ_i when κ is identified as the Karman constant.

In the outer layer, or wake region, a Clauser form of the eddy viscosity is employed

$$\epsilon_o=\alpha u_e \delta_k^* \gamma \tag{10}$$

Aguilar permits the coefficient α to be Reynolds number dependent, so that

$$\alpha=\begin{cases}0.0168 & R_{\theta_k}\geq 5000\\ 0.0168[1.55/(1+\tilde{\pi})] & R_{\theta_k}<5000\end{cases} \tag{11}$$

where

$$\tilde{\pi}=0.55[1-\exp(-0.243\beta^{1/2}-0.398\beta)] \tag{12}$$

and

$$\beta=(R_{\theta_k}/425)-1 \tag{13}$$

The subscript k in the displacement thickness δ_k^* and momentum thickness θ_k means these quantites are treated in a two-dimensional sense; for example,

$$\delta_k^*=\int_0^\delta\left(1-\frac{u}{u_e}\right)dy \tag{14}$$

Finally, the intermittency γ is represented by

$$\gamma=[1+5.5(y/\delta_x)^6]^{-1} \tag{15}$$

With ϵ_i or ϵ_o (from Eqs. (7) and (10), respectively) as scalar quantities, the components of the Reynolds stress tensor can be expressed as

$$-\overline{u_i'u_j'}=-\tfrac{2}{3}e\delta_{ij}+2\epsilon S_{ij} \tag{16}$$

where

$$S_{ij}=\tfrac{1}{2}(u_{i,j}+u_{j,i}) \tag{17}$$

Aguilar omitted the first term on the right-hand side of Eq. (16), which caused his model difficulty in predicting the normal stresses.

The Reynolds shear stresses in Eqs. (1-4) are given by Eqs. (16) and (17) as

$$-\overline{u'v'}=\epsilon\frac{\partial u}{\partial r} \tag{18}$$

$$-\overline{v'w'}=\epsilon\left(\frac{\partial w}{\partial r}-\frac{w}{r}\right) \tag{19}$$

Wilcox Rubesin Two-Equation Model (WR 2 Eq.)

The numerical code used in the DCW Industries two-equation method is a direct extension of the Price and Harris computer code[10] to include Eqs. (1-5). The two-equation

model introduced into the code is described in detail in Ref. 6, but the forms of the modeling equations in cylindrical coordinates are summarized here. The Reynolds shear stresses in Eqs. (1-4) employ Eqs. (18) and (19), except for the manner of evaluating the eddy viscosity. The Reynolds normal stresses are

$$\overline{u'^2}=e\left[\frac{2}{3}+\frac{4}{9}\frac{\left(\frac{\partial u}{\partial r}\right)^2}{\beta^*\omega^2+\left(\frac{\partial u}{\partial r}\right)^2+\left(\frac{\partial w}{\partial r}-\frac{w}{r}\right)^2}\right] \tag{20}$$

$$\overline{v'^2}=e\left[\frac{2}{3}-\frac{4}{9}\frac{\left(\frac{\partial u}{\partial r}\right)^2+\left(\frac{\partial w}{\partial r}-\frac{w}{r}\right)\left(\frac{\partial w}{\partial r}+\frac{w}{r}\right)}{\beta^*\omega^2+\left(\frac{\partial u}{\partial r}\right)^2+\left(\frac{\partial w}{\partial r}-\frac{w}{r}\right)^2}\right] \tag{21}$$

and

$$\overline{w'^2}=e\left[\frac{2}{3}+\frac{4}{9}\frac{\left(\frac{\partial w}{\partial r}-\frac{w}{r}\right)\left(\frac{\partial w}{\partial r}+\frac{w}{r}\right)}{\beta^*\omega^2+\left(\frac{\partial u}{\partial r}\right)^2+\left(\frac{\partial w}{\partial r}-\frac{w}{r}\right)^2}\right] \tag{22}$$

The sum of these equations is consistent with the definition

$$e=\tfrac{1}{2}(\overline{u'^2}+\overline{v'^2}+\overline{w'^2}) \tag{23}$$

For a two-dimensional boundary layer, the constants used in Eqs. (20-22) show that the normal Reynolds stresses take on the ratios

$$\overline{u'^2}:\overline{v'^2}:\overline{w'^2}=4:2:3 \tag{24}$$

The eddy viscosity in Eqs. (18) and (19) is given by

$$\epsilon=\gamma^* e/\omega$$

where the turbulence kinetic energy e and the pseudovorticity ω are found from the two partial differential equations

$$u\frac{\partial e}{\partial x}+v\frac{\partial e}{\partial r}=-\overline{u'v'}\frac{\partial u}{\partial r}-\overline{v'w'}\left(\frac{\partial w}{\partial r}-\frac{w}{r}\right)-\beta^*\omega e+\frac{1}{r}\frac{\partial}{\partial r}\left[r(\nu+\sigma^*\epsilon)\frac{\partial e}{\partial r}\right] \tag{25}$$

and

$$u\frac{\partial\omega^2}{\partial x}+v\frac{\partial\omega^2}{\partial r}=\gamma\frac{\omega^2}{e}\left[-\overline{u'v'}\frac{\partial u}{\partial r}-\overline{v'w'}\left(\frac{\partial w}{\partial r}-\frac{w}{r}\right)\right]-\left[\beta+2\sigma\left(\frac{\partial\ell}{\partial r}\right)^2\right]\omega^2+\frac{1}{r}\frac{\partial}{\partial r}\left[r(\nu+\sigma\epsilon)\frac{\partial\omega^2}{\partial r}\right] \tag{26}$$

The modeling coefficients appearing in these equations have the following values:

$$\left.\begin{aligned}&\beta=3/20,\ \beta^*=9/100,\ \sigma=\sigma^*=1/2\\&\gamma^*=1-(1-\lambda^2)\exp(-Re_T/R_e)\\&\gamma\gamma^*=\gamma_\infty[1-(1-\lambda^2)\exp(-Re_T/R_w)]\\&\gamma_\infty=10/9,\ \lambda=1/11,\ R_e=1,\ R_w=2\end{aligned}\right\} \tag{27}$$

ARAP Model (GYC RSE)

This method is based on a computer code developed by Sullivan.[7] The turbulence model is an outgrowth of the invariant tensor model of the complete set of Reynolds stresses originated by Donaldson.[8] Again, integrations are performed directly to the surface. The boundary-layer equations for the mean velocities in this method have been restricted to a body having a large radius relative to its boundary-layer thickness, neglecting the transverse curvature terms. Some consequences of this restriction are discussed later. On the other hand, the modeling equations for Reynolds stresses solved in the code contain terms including the effect of body radius. To be compatible with other models in the paper, the modeling equations are written here with just the terms thought to be important in this application.

$$u\frac{\partial\overline{u'^2}}{\partial x}+v\frac{\partial\overline{u'^2}}{\partial r}=-2\overline{u'v'}\frac{\partial u}{\partial r}-2a\frac{\nu}{\Lambda^2}\overline{u'^2}-\frac{2}{3}b\frac{q^3}{\Lambda}+\frac{2}{3}C_1\left[2\overline{u'v'}\frac{\partial u}{\partial r}-\overline{v'w'}\left(\frac{\partial w}{\partial r}-\frac{w}{r}\right)\right]+2C_2\frac{q}{\Lambda}(\overline{u'^2}-\frac{1}{3}q^2)+\frac{\partial}{\partial r}\left[(\nu+\sigma_1 q\Lambda)\frac{\partial\overline{u'^2}}{\partial r}\right] \tag{28}$$

$$u\frac{\partial\overline{v'^2}}{\partial x}+v\frac{\partial\overline{v'^2}}{\partial r}=4\overline{v'w'}\frac{w}{r}-2a\frac{\nu}{\Lambda^2}\overline{v'^2}-\frac{2}{3}b\frac{q^3}{\Lambda}-\frac{2}{3}C_1\left[\overline{u'v'}\frac{\partial u}{\partial r}+\overline{v'w'}\left(\frac{\partial w}{\partial r}+2\frac{w}{r}\right)\right]+2C_2\frac{q}{\Lambda}(\overline{v'^2}-\frac{1}{3}q^2)-2C_3\frac{\partial}{\partial r}\left[q\Lambda\frac{\partial\overline{v'^2}}{\partial r}\right]+\frac{\partial}{\partial r}\left[(\nu+3\sigma_1 q\Lambda)\frac{\partial\overline{v'^2}}{\partial r}\right] \tag{29}$$

$$u\frac{\partial\overline{w'^2}}{\partial x}+v\frac{\partial\overline{w'^2}}{\partial r}=-2\overline{v'w'}\left(\frac{\partial w}{\partial r}+\frac{w}{r}\right)-2a\frac{\nu}{\Lambda^2}\overline{w'^2}-\frac{2}{3}b\frac{q^3}{\Lambda}-\frac{2}{3}C_1\left[\overline{u'v'}\frac{\partial u}{\partial r}-2\overline{v'w'}\left(\frac{\partial w}{\partial r}+\frac{1}{2}\frac{w}{r}\right)\right]+2C_2\frac{q}{\Lambda}(\overline{w'^2}-\frac{1}{3}q^2)+\frac{1}{r^2}\frac{\partial}{\partial r}\left[(\nu+\sigma_1 q\Lambda)\frac{\partial r^2\overline{w'^2}}{\partial r}\right] \tag{30}$$

$$u\frac{\partial\overline{u'v'}}{\partial x}+v\frac{\partial\overline{u'v'}}{\partial r}=2\overline{u'w'}\frac{w}{r}-\overline{v'^2}\frac{\partial u}{\partial r}-2a\frac{\nu}{\Lambda^2}\overline{u'v'}-\frac{\partial}{\partial r}\left(\frac{1}{4}C_4\Lambda^2\frac{\partial u}{\partial r}\frac{\partial\overline{v'^2}}{\partial r}+C_3 q\Lambda\frac{\partial\overline{u'v'}}{\partial r}\right)+C_1\left(-\frac{w}{r}\overline{u'w'}+\overline{v'^2}\frac{\partial u}{\partial r}\right)+2C_2\frac{q}{\Lambda}\overline{u'v'}+\frac{\partial}{\partial r}\left[(\nu+2\sigma_1 q\Lambda)\frac{\partial\overline{u'v'}}{\partial r}\right] \tag{31}$$

$$u\frac{\partial\overline{v'w'}}{\partial x}+v\frac{\partial\overline{v'w'}}{\partial r}=2\frac{w}{r}\overline{w'^2}-\overline{v'^2}\left(\frac{\partial w}{\partial r}+\frac{w}{r}\right)-2a\frac{\nu}{\Lambda^2}\overline{v'w'}-\frac{1}{r}\frac{\partial}{\partial r}\left[\frac{1}{4}C_4r^2\frac{\partial\overline{v'^2}}{\partial r}\Lambda^2\frac{\partial}{\partial r}\left(\frac{w}{r}\right)+C_3q\Lambda\frac{\partial}{\partial r}(r\overline{v'w'})\right]$$

$$+C_1\left[v'^2r\frac{\partial}{\partial r}\left(\frac{w}{r}\right)+(\overline{v'^2}-\overline{w'^2})\frac{w}{r}\right]+2C_2\frac{q}{\Lambda}\overline{v'w'}+\frac{1}{r}\frac{\partial}{\partial r}\left[(\nu+2\sigma_1q\Lambda)\frac{\partial}{\partial r}(r\overline{v'w'})\right] \tag{32}$$

$$u\frac{\partial\overline{u'w'}}{\partial x}+v\frac{\partial\overline{u'w'}}{\partial r}=-\overline{u'v'}\left(\frac{\partial w}{\partial r}+\frac{w}{r}\right)-\overline{v'w'}\frac{\partial u}{\partial r}-2a\frac{\nu}{\Lambda^2}\overline{u'w'}+C_1\left(\overline{u'v'}\frac{\partial w}{\partial r}+\overline{v'w'}\frac{\partial u}{\partial r}\right)$$

$$+2C_2\frac{q}{\Lambda}\overline{u'w'}+\frac{1}{r}\frac{\partial}{\partial r}\left[(\nu+\sigma_1q\Lambda)\frac{\partial}{\partial r}(r\overline{u'w'})\right] \tag{33}$$

In these equations, Λ is a length scale of turbulence which has been assigned in an algebraic functional form as

$$\Lambda=\begin{cases}0.65(r-r_w) & r-r_w<0.26\delta_x\\ 0.17\delta_x & r-r_w>0.26\delta_x\end{cases} \tag{34}$$

The velocity scale q is related to the kinetic energy of turbulence as

$$q^2=2e \tag{35}$$

The mdeling coefficients were used with the following values;

$$\alpha=3.25,\quad b=0.125,\quad C_1=0,\quad C_2=-0.5,\quad C_3=-0.1,\quad C_4=0,\quad \sigma_1=0.1 \tag{36}$$

Equations (1-4) and (28-35) form a closed system for evaluating a turbulent boundary layer from the surface to its outer edge.

Wilcox-Rubesin Reynolds Stress Equation Model (WR RSE)

The same computer code described for use with the two-equation model was extended by Wilcox to include the full Reynolds stress equation model developed by Wilcox and Rubesin.[6] For brevity, the modeling equations for rotating flow in cylindrical coordinates are written in general form where i,j take on values of 1, 2, or 3.

$$u_1\frac{\partial}{\partial x}(\overline{u_i'u_j'})+u_2\frac{\partial}{\partial r}(\overline{u_i'u_j'})=-\overline{u_j'u_2'}\left(\delta_{j1}\frac{\partial u_1}{\partial r}+\delta_{j3}\frac{\partial u_3}{\partial r}\right)+\overline{u_i'u_3'}\delta_{j2}\frac{u_3}{r}-\overline{u_j'u_2'}\left(\delta_{i1}\frac{\partial u_1}{\partial r}+\delta_{i3}\frac{\partial u_3}{\partial r}\right)+\overline{u_j'u_3'}\delta_{i2}\frac{u_3}{r}-\frac{2}{3}\beta^*\omega e\delta_{ij}$$

$$-\lambda^*\omega[\overline{u_i'u_j'}-\frac{2}{3}e\delta_{ij}]+\frac{1}{2}\left[(\overline{u_1'u_i'}\delta_{j2}+\overline{u_1'u_j'}\delta_{i2}+\overline{u_i'u_2'}\delta_{j1}+\overline{u_j'u_2'}\delta_{i1})\frac{\partial u_1}{\partial r}+(\overline{u_j'u_2'}\delta_{3i}+\overline{u_j'u_3'}\delta_{i2}+\overline{u_i'u_2'}\delta_{3j}+\overline{u_i'u_3'}\delta_{j2})\left(\frac{\partial u_3}{\partial r}-\frac{u_3}{r}\right)\right]$$

$$-\frac{2}{3}\delta_{ij}\left[\overline{u_1'u_2'}\frac{\partial u_1}{\partial r}+\overline{u_2'u_3'}\left(\frac{\partial u_3}{\partial r}-\frac{u_3}{r}\right)\right]-\frac{2}{3}e\left[(\delta_{j2}\delta_{i1}+\delta_{i2}\delta_{j1})\frac{\partial u_1}{\partial r}+(\delta_{j2}\delta_{3i}+\delta_{i2}\delta_{j3})\left(\frac{\partial u_3}{\partial r}-\frac{u_3}{r}\right)\right]$$

$$-\frac{u_3}{r}[\delta_{j3}\overline{u_i'u_2'}-\delta_{j2}\overline{u_i'u_3'}+\delta_{i3}\overline{u_2'u_j'}-\delta_{i2}\overline{u_j'u_3'}]+\frac{1}{r}\frac{\partial}{\partial r}\left[r(\nu+\sigma^*\epsilon)\frac{\partial\overline{u_i'u_j'}}{\partial r}\right] \tag{37}$$

The modeling coefficients are

$$\beta=3/20,\quad \beta^*=9/100,\quad \sigma=\sigma^*=1/2$$

$$\lambda^*=\lambda^*_\infty[1-(1-\lambda^2)\exp(-Re_T/R_e)]$$

$$\frac{\gamma}{\lambda^*}=\frac{\gamma_\infty}{\lambda^*_\infty}[1-(1-\lambda^2)\exp(-Re_T/R_w)]$$

$$\lambda^*_\infty=\left[\frac{9}{2}-\frac{5}{2}\exp(-5\chi)\right]\beta^*$$

$$\gamma_\infty=\frac{13}{11},\quad \lambda=1/14,\quad R_e=1,\quad R_w=3$$

$$\chi=\sqrt{\left[\left(\frac{\partial u}{\partial r}\right)^2+\left(\frac{\partial w}{\partial r}-\frac{w}{r}\right)^2\right]/\beta^*\omega^2} \tag{38}$$

The eddy diffusivity in Eq. (37) is given by

$$\epsilon=e/\omega$$

where Eq. (23) is used to define e and ω is obtained from Eq. (26).

Discussion

It is informative to consider the genesis of the turbulence models described earlier before making detailed comparisons of the computed results and the experimental data.

The Aguilar mixing length model is an extrapolation of past mixing length and eddy viscosity models. These models compose the boundary layer into an inner region and an outer region. Besides the viscosity of the fluid, the inner region depends on two turbulence modeling coefficients that are defined by law-of-the-wall plots of data. The Karman constant follows from the slope of the logarithmic portion of the wall "law," and the van Driest damping constant is established by its level. These coefficients are κ of Eq. (6) and the factor 26 in Eq. (9). The outer region, the "wake," is independent of molecular viscosity and can be represented as having a uniform eddy viscosity proportional to the boundary-layer displacement thickness, Eq. (10). The constant α in this equation follows from mean velocity data correlations. The intermittency term appearing in Eq. (10), though helpful from a numerical point of view, is not critical to the tur-

bulence modeling. For planar boundary layers that have slowly varying boundary conditions, the Aguilar model is merely a systematic means of interpolating and extrapolating experimental data and can be expected to provide accurate predictions. In the current application, this model should yield good results upstream of the junction between the stationary and rotating cylinders. Also, far downstream on the rotating cylinder where the circumferential boundary layer is fully established relative to the axial boundary layers, the collateral condition, a model that assumes equilibrium between the mean motions and the turbulence should yield reasonable results, provided the effects of the circumferential flow on the turbulence are properly introduced. Unfortunately, as will be shown later, the experiments considered here were not extended sufficiently downstream to test this latter point with certainty. Immediately downstream of the junction, however, a model that assumes equilibrium between mean flow and turbulence is suspect, and it is in this region that the more complex models were expected to show improvement over the Aguilar model.

Examination of the Reynolds stress modeling equations presented earlier reveals that they contain about 10 modeling coefficients, in addition to assumed functional forms for the modeled terms of dissipation, diffusion, and redistribution between the Reynolds stresses. To establish such a large number of modeling coefficients, it is necessary to draw upon a variety of experiments, each emphasizing a different aspect of the turbulence models. For example, the coefficient for the viscous dissipation of Reynolds stress is usually established from data on the decay of homogeneous, isotropic turbulence. This leads to a model that results in the decay of only normal Reynolds stresses; for example, the terms with β^* in Eq. (37). The GYC RSE code is broader in this regard; it allows for the decay of off-diagonal Reynolds stresses and the effects of low-turbulence Reynolds number (the coefficient a). Coefficients for the interaction of the individual Reynolds stresses, C_1 and C_2, come either from experiments on sheared homogeneous turbulent flows or from asymptotic examinations of the modeling equations in the logarithmic portion of the wall region of an attached planar boundary layer. Because these latter methods do not give exactly the same values of the modeling coefficients, some compromise between the two is usually made. Although the GYC RSE code is particularly versatile in the choice of modeling constants, in the computations here the effect of mean strain on the correlation of the pressure and rate of strain fluctuations has been eliminated by setting $C_1 = 0$, in order to bring about close conformity between the GYC RSE and WR RSE codes for $u'v'$ terms (see Ref. 11).

Other coefficients (e.g., the diffusion terms) are found by optimizing the calculations against boundary-layer data. In general, because these models use data from a variety of flowfields and depend on approximate functional forms for the modeling terms, they are not as fine-tuned for equilibrium boundary layers as are the mixing length models. Thus, for equilibrium flows, the newer models cannot be expected to be better than the mixing length models. Modelers are content when their more complex models fit the simple flowfields to about 5%. The value of the more complex models is their ability to account for changes in boundary conditions so sudden as to disrupt the equilibrium between the mean and turbulent motions, and to permit computations for a variety of flowfields without introducing new assumptions. Since the experiments considered here are examples of a sudden change in boundary conditions, it would be expected that the newer models would fit the data over the upstream portion of the rotating cylinder better than the mixing length model.

The computed results of the axial and transverse mean velocity profiles, compared with the data of Bissonnette and Mellor[2] and Lohmann[3] for the lower rotation rates in each experiment, are shown in Figs. 2a and 2b. The development of the boundary layers after the imposition of the strain is shown

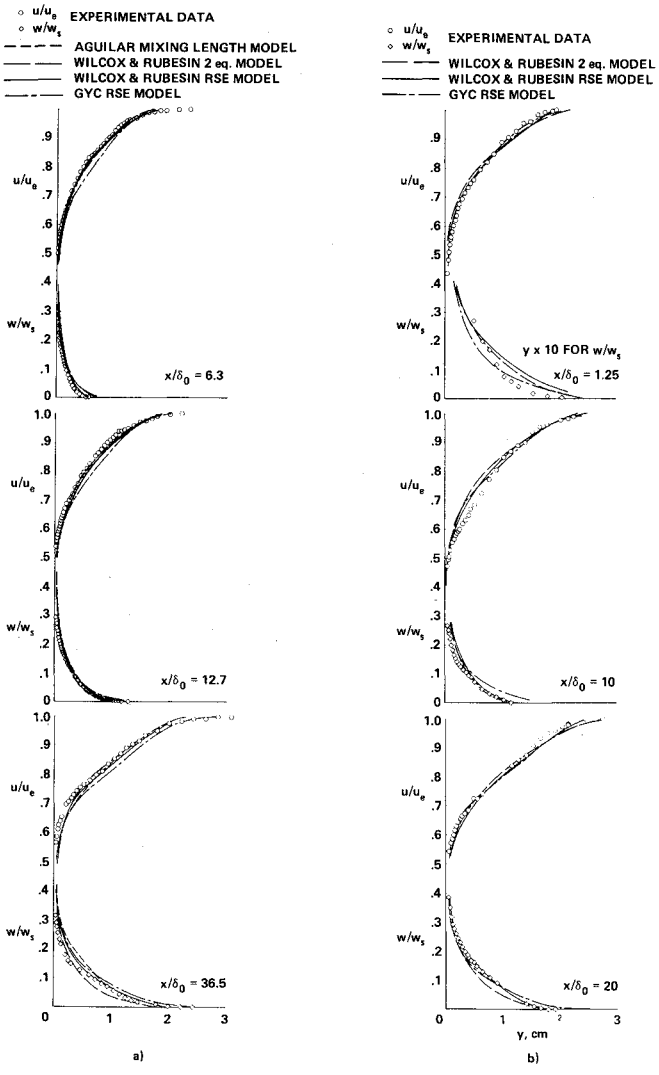

Fig. 2 Comparison of mean velocity profiles from experiment and computation: a) experiment of Bissonnette and Mellor, $\Omega = 0.936$; b) experiment of Lohmann, $\Omega = 1.45$.

at three representative stations. Even though the flow immediately downstream of the junction is of primary interest here, the data from the first station of the Bissonnette and Mellor experiment were not used because the measurements in the transverse boundary layer at this station were inconsistent with the rest of the stations. All the models show reasonable agreement with both the axial and transverse data. Surprisingly, the simple mixing length model predicts the Bissonnette and Mellor mean velocity profiles with as good agreement as the more general models. The models show the largest quantative difference for the transverse boundary layer. These differences are consistent from station to station and for the two rotation speeds. Because the data of the two experiments are shifted slightly in opposite directions relative to the computations, it is difficult to select the model that best fits the data. This is especially so because some models fit the data best near the surface, whereas others are best near the outer edge of the boundary layer.

In Fig. 6 of Ref. 3, Lohmann shows a comparison of the spinning and nonspinning boundary-layer axial velocity profile data. The axial mean velocity in the spinning case has a deficit near the center of the transverse boundary layer. This region moves outward within the axial boundary layer as the transverse boundary layer grows. The models pick up this change in the axial mean velocity profile, but as seen in the $\chi/\delta_0 = 10$ station, they underpredict the magnitude of the effect seen from the experimental data.

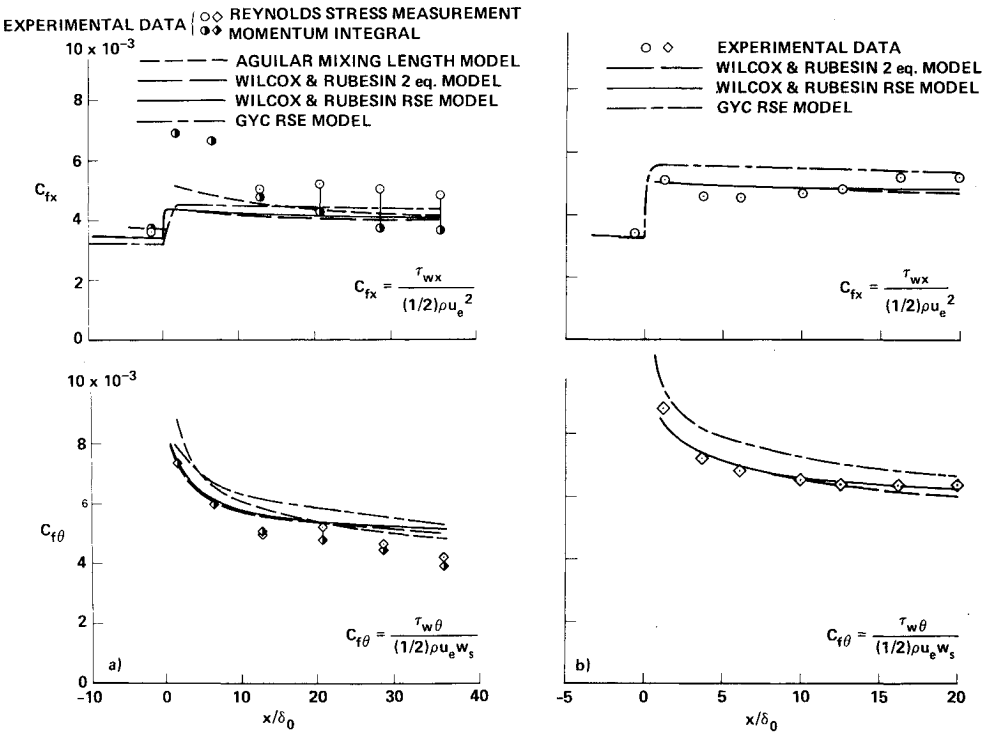

Fig. 3 Comparison of measured and computed axial and transverse skin-friction coefficients: a) experiment of Bissonnette and Mellor, $\Omega = 0.936$; b) experiment of Lohmann, $\Omega = 1.45$.

Data obtained at higher rotation rates in each of the experiments were also examined. The data of Lohmann at $\Omega = 2.2$ were presented quite accurately by the WR 2 Eq., WR RSE, and GYC RSE computations, the measured axial velocity being only slightly fuller. The high rotation-rate data of Bissonnette and Mellor, $\Omega = 1.80$, for both the axial and transverse mean velocities were much fuller than any of the computational methods, but especially fuller than the mixing length method. Too much credence cannot be given to this result, however, since these data are not consistent with even higher rotation-speed data by Lohmann.

The comparison of the calculated and experimental axial and transverse skin-friction coefficients are shown in Figs. 3a and 3b. The form of the transverse skin-friction coefficient used assures $C_{fx} = C_{f\theta}$ at the collateral condition of a thin boundary layer where $(1 - w/w_s) = u/u_e$. These experimental data are inferred quantities, as the skin friction was not measured directly in either of the experiments. Bissonnette and Mellor extrapolated their hot-wire Reynolds shear stress data to the surface for all stations except the first two near the junction, where the uncertainty in the data did not allow this procedure. They also evaluated skin friction by integrating the mean axial and transverse velocities in integral momentum equations. The discrepancy between the data obtained from the two methods is rather large, particularly for the axial direction (see Fig. 3a).

Lohmann's skin-friction data were obtained from Clauser plots on the assumption that the law-of-the-wall holds when expressed in the resultant velocity relative to the surface of the rotating cylinder and the resultant skin friction. The resultant skin-friction was then split into axial and transverse components with the measured mean velocity direction in the limit near the wall. This method becomes questionable near the junction where the mean velocity is highly skewed because of the thin transverse boundary layer. Further, the resultant mean velocity data showed a very narrow semilogarithmic region which makes the use of Clauser plots rather inaccurate. Sufficiently far downstream of the junction, however, the data follow the law-of-the-wall well and are consistent with the hot-wire Reynolds shear stress measurements.

Certain trends are expected in these data. After the junction, the axial skin-friction coefficient is expected to rise toward a higher value because of the additional strain introduced by the transverse motion. This effect is opposed by the growth of the boundary layer which causes a gradual decrease of the skin friction downstream. The overall behavior of the boundary layer, then, reflects the rates of these competing processes. The transverse skin-friction coefficient is expected to have a very large value just downstream of the junction where the transverse boundary layer is initiated. This is analogous to the behavior of a thermal boundary layer just downstream of a surface temperature jump. The transverse skin-friction coefficient then falls with downstream distance toward the value of the axial skin-friction coefficient as the collateral condition is approached. Figures 3a and 3b indicate general agreement with these expectations for both the computations and the data. Specifically, upstream of the junction, differences are seen in Fig. 3a among the various models, even though care was taken to match the experimental momentum thickness of the data at that station. The fine-tuned mixing length model passes through the data, whereas the second-order models predict values that are slightly lower than the data. These latter models, however, fit Lohmann's data quite well, upstream of the junction. The Bissonnette and Mellor data immediately after the junction show that the predictions of the axial skin friction are much lower than the somewhat uncertain momentum integral data. The values of $C_{f\theta}$ based on the Reynolds stress measurements unexpectedly fall below the similarly obtained C_{fx} data. This behavior leads one to favor the Lohmann skin-friction data as standards for comparison with the computations. Lohmann's data immediately downstream of the junction are much lower than the Bissonnette and Mellor data. The more reliable axial skin-friction coefficients at the downstream stations show a gradual increase for some distance after the junction. The skin-friction data appear to reach a maximum near $\chi/\delta_0 = 20$ although these data do not extend sufficiently downstream to define a maximum unambiguously. The Bissonnette and Mellor Reynolds stress data show a similar position of a maximum skin friction. A comparison between the computations and Lohmann's data indicates that the models do not define the rate processes properly. They show such a rapid rise in the turbulence that the position of maximum axial skin

friction resulting from the competing mechanisms of turbulence generation and boundary-layer growth occurs much too quickly. Downstream of this point, the continued promotion of turbulence does not permit the usual reduction caused by boundary-layer growth and the effects combine to yield a very slow decrease in C_{fx}. It is apparent that the second-order turbulence models, in their present state of development, are not yielding proper rates for the relaxation processes driven by shearing motion. Although the Lohmann data has been stressed here, the Bissonnette and Mellor Reynolds stress data would yield similar conclusions regarding the rate process of the second-order models. Further, the mixing length model, always keeping the turbulence and mean motion in equilibrium, shows the poorest dynamic behavior: it yields a much greater rise and a more rapid fall-off of the axial skin friction than either the other models or the data.

For the transverse skin friction, the mixing length model predicts the highest rise downstream of the junction. Generally, all the models overpredict the Bissonnette and Mellor data by about 20%. Lohmann's data are similarly overpredicted by the GYC RSE code, whereas they are predicted quite well by the WR RSE model. The two-equation model departs from the data at the farthest downstream stations. It appears that the latter model has equilibrated faster than the WR RSE. A larger slope than shown was expected for the GYC RSE model because of the absence of transverse curvature effects; however, these effects appear to have been compensated by the slower redistribution mechanisms in this model. (Just after the junction, rate of rise in GYC RSE is slower than in WR 2 Eq. or in WR RSE, see Fig. 3a.)

Since the functional forms of the terms modeling the pressure rate of strain correlations are approximations, it cannot be expected that each of the components of the Reynolds stress tensor can be predicted with equal accuracy. For example, in the boundary layer of a flat plate, the GYC RSE program is known to yield $\overline{w'^2} = \overline{v'^2}$ (Ref. 11), whereas $\overline{w'^2} = 1.5\,\overline{v'^2}$ is closer to the data. The modeling coefficients have been adjusted to yield the best predictions for the most important component of the Reynolds stress, namely the shear stress, at the expense of accuracy of the normal stresses. In the present study, transverse shearing introduces two additional shear stresses nonexistent in the two-dimensional boundary layer, although only one of them, $\overline{v'w'}$, plays an important role in the transverse momentum equation. Figures 4-6 demonstrate the ability of the Reynolds stress models to define the components of the Reynolds stress tensor under conditions of transverse shear.

Figure 4 shows $\overline{u'v'}$ profiles across the boundary layers at the farthest downstream station in both experiments. The data were obtained with a rotated slant wire in both experiments. All the computations underpredict the Bissonnette and Mellor data in the inner one-third of the boundary layer. This is reflected in the surface skin-friction data (open circles) apthis station (refer to Fig. 3). For the data of Lohmann, the models all yield reasonable predictions of the Reynolds shear stress and the surface skin friction. The order of the individual models and the data are generally consistent for both the Reynolds shear stress and the surface skin friction. The transverse Reynolds shear stress $\overline{v'w'}$ bears as much significance as the axial Reynolds shear stress $\overline{u'v'}$, in the presence of the transverse strain. Because experimental data on $\overline{v'w'}$ are suspect near the junction, the data are compared with the predictions at their farthest downstream stations. Figure 5a shows the results of Bissonnette and Mellor's experiment. Fair agreement in the outer region is achieved by both of the RSE models, but the experimental data show a rapid decrease in magnitude toward the wall. This phenomenon is not captured by the predictions. It must be noted, however, that the experimental data taken at different axial positions showed trends inconsistent with these trends near the wall. Comparison with the $\overline{u'v'}$ data suggests the error in $\overline{v'w'}$ was in defining the direction of the shear stress measured by a single slant wire near the wall. The peak value in $\overline{v'w'}$ seen in the Lohmann's experiment, Fig. 5b, is predicted reasonably well by the three models, and the agreement is consistent with the prediction of the transverse skin friction. However, the data, which appear to be consistent with $\overline{u'v'}$ data, show a much fuller profile than predicted. The failure to predict the fullness of the inner region does not seem to have a first-order effect on the transverse mean velocity profile (refer to Fig. 2).

When the boundary-layer thickness remains small, the radial Reynolds shear stress $\overline{u'w'}$ does not play a direct role in the mean momentum equations because of the axisymmetry of the flow [see Eqs. (1-4)]. Nevertheless, the measured magnitude of the stress is comparable to the other components of shear stresses. In the turbuence modeling equations, the redistribution term in the Reynolds shear stress equations generally contains the radial Reynolds shear stress, which in turn affects the behavior of the boundary layer. Launder and Morse applied the Launder, Reece, and Rodi model to the swirling jet (Ref. 12) and found that the predicted $\overline{u'w'}$ had the wrong sign when compared with the experimental data. A comparison of the $\overline{u'w'}$ data and the Reynolds stress models used here showed that the correct sign of the quantity is predicted, but the quantitative agreement is generally poor, particularly in case of the WR RSE model.

The existence of high transverse strain gives rise to the production of turbulence and alters the balance among $\overline{u'^2}$, $\overline{v'^2}$ and $\overline{w'^2}$. Since both Reynolds stress equation models yield similar results, for simplicity only the results of the WR RSE model will be discussed. Near the junction, both experimental and predicted normal stress profiles showed two

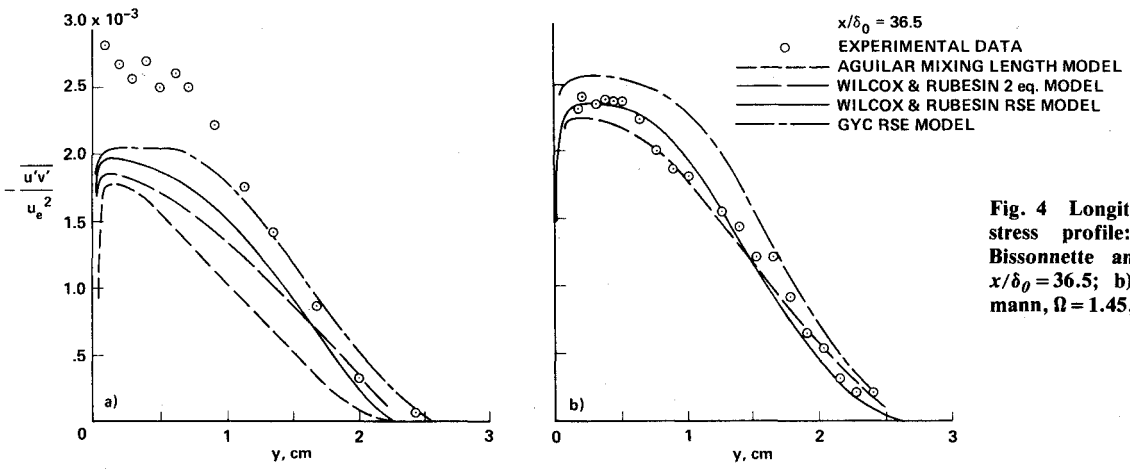

Fig. 4 Longitudinal Reynolds shear stress profile: a) experiment of Bissonnette and Mellor, $\Omega = 0.936$, $x/\delta_0 = 36.5$; b) experiment of Lohmann, $\Omega = 1.45$, $x/\delta_0 = 20$.

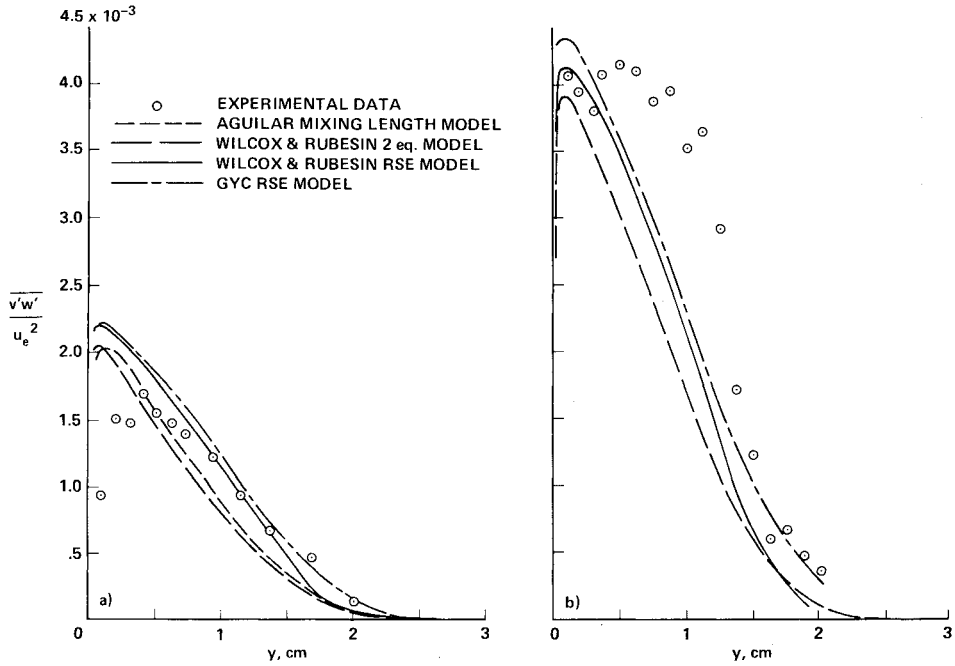

Fig. 5 Transverse Reynolds shear stress profile: a) experiment of Bissonnette and Mellor, $\Omega = 0.936$, $x/\delta_0 = 36.5$; b) experiment of Lohmann, $\Omega = 1.45$, $x/\delta_0 = 20$.

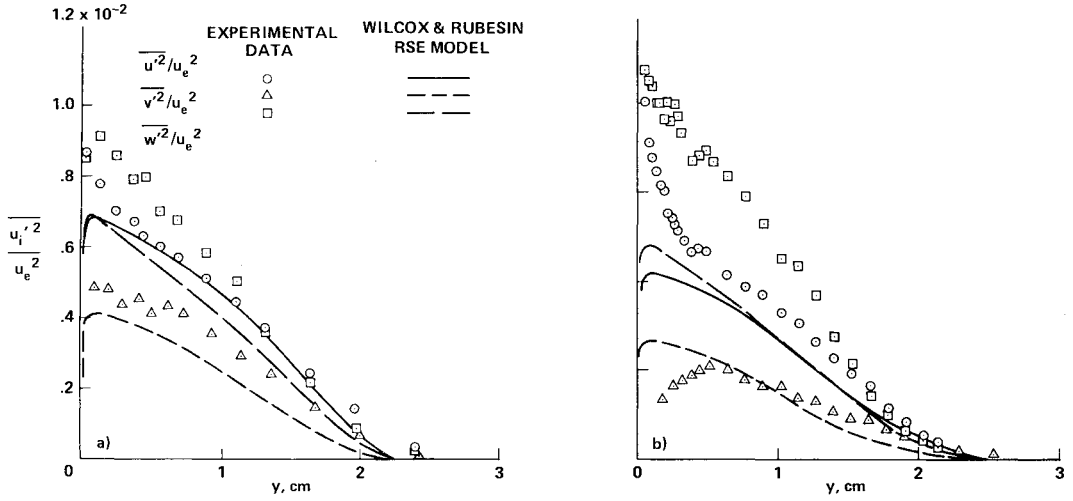

Fig. 6 Reynolds normal stress profiles: a) experiment of Bissonnette and Mellor, $\Omega = 0.936$, $x/\delta_0 = 36.5$; b) experiment of Lohmann, $\Omega = 1.45$, $x/\delta_0 = 20$.

distinctive regions within the boundary layer. The inner region, containing the transverse boundary layer, has sharply rising axial and transverse components $\overline{u'^2}$ and $\overline{w'^2}$ toward the wall. The outer region remains unchanged from the nonsurface rotation case. While the agreement of the prediction with the data in the outer region is good, the increase in the turbulent intensity near the wall due to the transverse shear was underpredicted. At downstream stations, the highly turbulent region diffuses throughout the entire boundary layer. Here the re-equilibration process among the stress components is considered to have reached its asymptotic state. Therefore, to assess the asymptotic behavior of the models, the predictions of the farthest downstream position measured by Bissonnette and Mellor and by Lohmann are shown in Figs. 6a and 6b. In Fig. 6a, the high magnitude of the transverse component of the normal stresses caused by the imposed transverse strain is qualitatively reflected in the prediction. However, all three components of the normal stresses are underpredicted; particularly, the peak of the transverse component of Reynolds normal stress is missed by 30%. Bissonnette and Mellor's high rotation-rate case was predicted even more poorly. In Fig. 6b, the transverse component $\overline{w'^2}$ of the Reynolds normal stress is missed by a factor of nearly 2. Incidentally, the maximum point occurring in measured $\overline{v'^2}$ away from the wall is believed to be caused by probe interference because the hot wire spans the highly skewed mean velocity near the wall. The predictions for higher rotation rates show similar shortcomings. In all cases, the models were found deficient in predicting the redistribution process among the components of the Reynolds normal stresses; the fact that the mean velocity and surface skin friction are reasonably predicted by the models in spite of the poor predictions of the Reynolds normal stresses suggests that the models were tuned so that satisfactory predictions could be made of these quantities normally of primary interest. This discrepancy in prediction should not be dismissed. It is suspected that these models may prove to be less than sufficient in predicting fully three-dimensional flows or regions near separation, where the interaction among all components of Reynolds stress is expected to play a significant role.

A common assumption made in the computation of three-dimensional boundary layers is that the eddy viscosity is a scalar quantity, equal in the axial and transverse momentum equations. The present investigation provides the opportunity to test this hypothesis against the data of the experiments and the Reynolds stress models. For this purpose, the eddy viscosities compared are

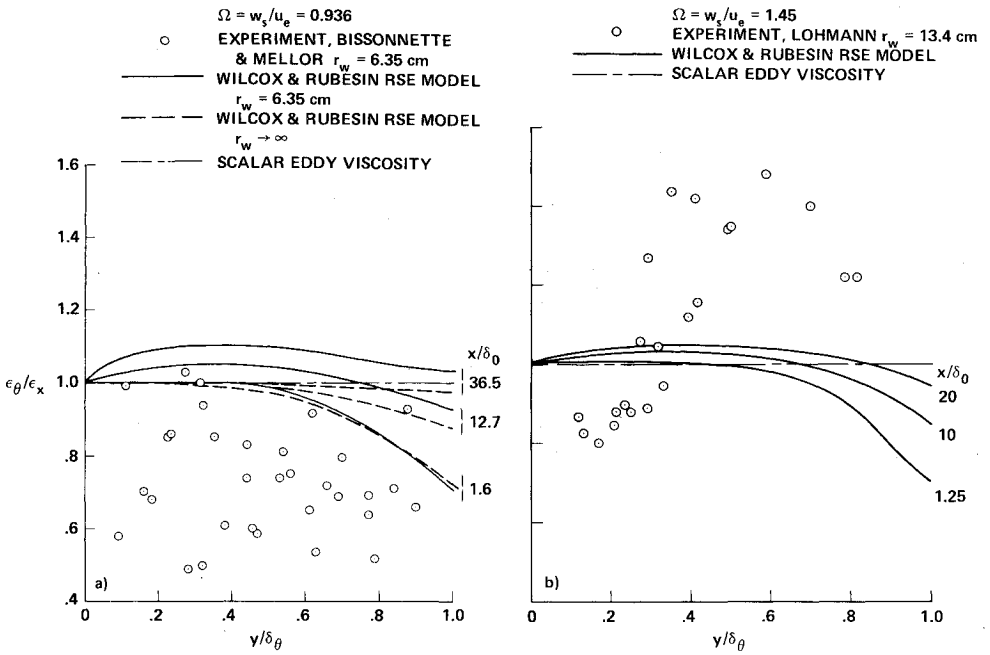

Fig. 7 Ratio of eddy viscosity coefficients: a) experiment of Bissonnette and Mellor, Ω = 0.936; b) experiment of Lohmann, Ω = 1.45.

$$\epsilon_x = -\overline{u'v'} \Big/ \frac{\partial u}{\partial r} \qquad \epsilon_\theta = -\overline{v'w'} \Big/ \left(\frac{\partial w}{\partial r} - \frac{w}{r}\right)$$

The ratio $\epsilon_\theta/\epsilon_x$ for the two experiments is shown in Figs. 7a and 7b. Data are plotted for all axial stations, since they failed to show any definite trend at various axial stations. Immediately noticeable is the large scatter of the data in the individual experiments. The Bissonnette and Mellor data scatter around a value of $\epsilon_\theta/\epsilon_x = 0.7$. The Lohmann data show values smaller than unity toward the surface but values significantly larger than unity near the center of the transverse boundary layer. The uncertainties in the data shown here reflect the inaccuracies inherent in differentiating mean velocity data and in the shear stress measurements. Despite the shortcomings of the Reynolds stress models, their strengths in predicting the shear stresses and mean velocities allow their use in assessing $\epsilon_\theta/\epsilon_x$. The WR RSE model was chosen to make this test for these conditions because it accounts for the effects of transverse curvature.

The eddy viscosity ratio computed from the WR RSE model shows a deviation from the scalar eddy viscosity condition in the outer region of the transverse boundary layer immediately downstream of the imposition of sudden strain. Further downstream, the computed value approaches the value of unity. At the farthest downstream axial station, the ratio of eddy viscosity coefficients overshoots unity; this is the effect of the thickness of the boundary layer relative to the body radius. In Fig. 7b, the amount of the overshoot is smaller, as the Lohmann experiment experiences fewer transverse curvature effects. Finally, the dashed lines of Fig. 7a represent the case of infinite radius of curvature; the ratio approaches unity monotonically.

Although the WR RSE model allows misalignment between the mean velocity strain vector and the Reynolds stress vector, the computed results show a fairly small deviation from the scalar eddy viscosity condition. Also, the two scalar eddy viscosity models predicted the mean flow data as well as the more complex models. Therefore, it appears that the transverse boundary layer grows within the axial boundary layer with a common transport mechanism.

Concluding Remarks

A comparison has been made between computations based on two different Reynolds stress equation models and data from two boundary-layer experiments designed expressly to define the rates of interaction between the components of the Reynolds stress tensor after a sudden imposition of a transverse shear. Comparisons were also made with computations based on models that ignore the interaction mechanism of the Reynolds stresses but deal directly with the shear stresses. These latter models, a first-order algebraic mixing length model and a second-order two-equation model, employ the additional assumption that the eddy viscosity is a scalar and is equal locally in the axial and transverse boundary layers.

The comparison indicates the simple mixing length model yields results in general agreement with the gross features of the mean flow. The second-order models, whether the two-equation eddy viscosity model or either of the two Reynolds stress equation models, showed comparison that are somewhat, but not dramatically, better than the simpler model. The reason for the limited improvement of the second-order models seems to be their too rapid rate of response to the transverse shear. Furthermore, near a position where the rotating boundary layer has equilibrated, the Reynolds stress equation models fail to represent the distribution of the normal stresses, $\overline{u'^2}$, $\overline{u'^2}$ and $\overline{w'^2}$, accurately. It appears that the reasonable representation of the shear stresses by these Reynolds stress equation models results not from an accurate representation of the physics of turbulence but rather from model tuning that emphasized the more important Reynolds shear stresses in establishing the mean flow. It is noted that these same Reynolds stress equation models represent the normal stresses quite well in homogeneous turbulent flows that are strained in normal directions. Shearing strain does not seem to be handled properly in the models. Further development of Reynolds stress equation models is required. Unfortunately, the data in the experiments considered here were least accurate just after the onset of the transverse shear where the rate processes are most controlling. In addition, the data did not extend sufficiently downstream to define the boundary-layer characteristics in equilibrium with the transverse shear. This equilibrium is particularly important to turbulence modeling because it permits the powerful tool of asymptotic analysis to be utilized in establishing the relative distributions of the Reynold stresses.

Finally, the results of the computations and data shown here demonstrate that the assumption in engineering computations of a scalar eddy viscosity, equal in magnitude in the axial and transverse direction, is reasonable.

References

[1]Patel, V. C. and Nash, J. F., "Recent Advances in the Calculation of Turbulent Boundary Layers: Three-Dimensional and Unsteady Flows," *Proceedings of the Lockheed-Georgia Co. Viscous Flow Symposium*, LG77ER044, June 22-23, 1976.

[2]Bissonnette, L. R. and Mellor, G. L., "Experiments on the Behavior of an Axisymmetric Turbulent Boundary Layer with a Sudden Circumferential Strain," *Journal of Fluid Mechanics*, Vol. 63, Part 2, April 1974, pp. 369-413. (Also Ph.D. thesis by L. R. Bissonnette, Princeton University, 1970.)

[3]Lohmann, R. P., "The Response of a Developed Turbulent Boundary Layer to Local Transverse Surface Motion," *Transactions of ASME, Journal of Fluids Engineering*, Vol. 98, Sept. 1976, pp. 354-363. (Also Ph.D. thesis, University of Connecticut, 1974.)

[4]Aguilar, R., "A Numerical Analysis of Turbulent Flow Along an Abruptly Rotated Cylinder," Ph.D. thesis, Virginia Polytechnic Inst. and State University, 1976.

[5]Cebeci, T. and Smith, A.M.O., *Analysis of Turbulent Boundary Layers*, Academic Press, New York, N.Y., 1974.

[6]Wilcox, D. C. and Rubesin, M. W., "Progress in Turbulence Modeling for Complex Flowfields, Including Effects of Compressibility," (to be published as NASA TP).

[7]Sullivan, R. D., "GYC: A Program to Compute the Turbulent Boundary Layer on a Rotating Cone," ARAP Working Paper No. 76-2, Aug. 1976.

[8]Donaldson, C. duP., "Calculation of Turbulent Shear Flows for Atmospheric and Vortex Motions," *AIAA Journal*, Vol. 10, Jan. 1972, pp. 4-12.

[9]Cebeci, T., "Eddy-Viscosity Distribution in Thick Axisymmetric Turbulent Boundary Layers," *Transactions of ASME, Journal of Fluids Engineering*, June 1973, pp. 319-326.

[10]Price, J. M. and Harris, J. E., "Computer Program for Solving Compressible Nonsimilar Boundary-Layer Equations for Laminar, Transitional, and Turbulent Flows of a Perfect Gas," NASA TM X-2458, April 1972.

[11]Rubesin, M. W., Crisalli, A. J., Lanfranco, M. J., and Acharya, M., "A Critical Evaluation of Invariant Second-Order Closure Models for Subsonic Boundary Layers," Paper 4A, Symposium on Turbulent Shear Flows, Pennsylvania State University, University Park, Penn., April 18-20, 1977.

[12]Launder, B. E. and Morse, A., "Numerical Prediction of Axisymmetric Shear Flows with a Second-Order Reynolds Stress Closure," Paper 4C, Symposium on Turbulent Shear Flows, Pennsylvania State University, University Park, Penn., April 18-20, 1977.